

Multifunctional carbon armor: Synchronously improving oxygen reaction kinetics, mass transfer dynamics, and robustness of transition metal alloy based hybrid catalyst

Lei Zhang^{a,1}, He Jiang^{b,1}, Min Tang^{c,1}, Ying Jiang^c, Bing Tang^d, Hao Tan^{d,*}, Yuan Kong^{e,*}, Haibo Hu^{a,*}

^a School of Materials Science and Engineering, Anhui University, Hefei 230601, PR China

^b School of Chemistry, University of Southampton, Southampton SO17 1BJ, UK

^c State Key Laboratory of Silicon and Advanced Semiconductor Materials and Center of Electron Microscopy, School of Materials Science and Engineering, Zhejiang University, Hangzhou 310027, PR China

^d National Synchrotron Radiation Laboratory, University of Science and Technology of China, Hefei 230029, PR China

^e Hefei National Laboratory for Physical Sciences at the Microscale and Department of Chemical, Physics and Synergetic Innovation Center of Quantum Information and Quantum Physics, University of Science and Technology of China, Hefei 230029, PR China



ARTICLE INFO

Keywords:

Bifunctional oxygen catalyst
Zinc-air battery
Transition metal alloy
Multifunctional carbon armor
Single-atom catalysis

ABSTRACT

Construction of robust protective cover on delicate active sites is a frequently-used scheme to enhance the durability of air-cathode catalyst working in harsh environment, thus the lifespan of rechargeable Zinc-air batteries (ZABs). Paradoxically, this would degrade the activity due to the constricted accessibility of active sites to reactants. Herein, carbon nanotubes with abundant mesoporous defects and Fe-N₄ species were elaborately designed to be multifunctional protective armor to encapsulate Ni₃Fe nano-alloys (Ni₃Fe@CNTs/Fe-N₄) for bifunctional oxygen electrocatalyst. In/ex-situ spectroscopy analysis and theoretical calculations reveal that the constructed mesoporous carbon defects effectively facilitate the multiphase mass transfer and the oxygen evolution reaction kinetics via strong electrons coupling with packaged Ni₃Fe nano-alloys. Meanwhile, the synchronously introduced Fe-N₄ moieties could serve as oxygen reduction active sites. Thus, the obtained Ni₃Fe@CNTs/Fe-N₄ hybrid electrocatalyst simultaneously exhibits remarkable bifunctional catalytic activity ($E_{1/2}=0.86/E_{j=10}=1.59$ V vs RHE) and durability over 450 h in the chronoamperometric test at 1.59 V, endowing the assembled Zn-air batteries (ZABs) with a high power density (150 mW cm⁻²) and lifespan (307 h), much better than that employing benchmark Pt/C+RuO₂ mixed catalyst. This work demonstrates an innovative design route for the multifunctional armor to concurrently enhance the durability, activity and robustness of air-cathode-catalyst for ZABs.

1. Introduction

Rechargeable Zinc-air batteries (ZABs) are a focus of research for grid-level energy storage due to their low cost, high theoretical energy density (1353 Wh kg⁻¹) rooting in the utilized Zn metal anode and semi-open structure, along with the inherent operational safety provided by aqueous electrolytes [1–5]. Nevertheless, the actual deployment of ZABs is still severely restricted by their low energy efficiency and inadequate lifespan due to the sluggish oxygen reaction kinetics on the air cathode and poor stability of the loaded catalyst [6,7]. Moreover, the high cost of

the currently employed noble metal based air cathode catalysts also greatly hinders their large-scale application [8–10]. In this context, design and fabrication of cost-effective air cathode catalyst with both high catalytic activity and stability is of great significance for the development of ZABs [11–14].

Encouragingly, over the past decades, various non-noble metal based air cathode catalyst with high catalytic activity have been developed such as heteroatom-doped carbon, transition metal oxides and metal nitrogen-carbon catalysts, etc [15–23]. Specifically, the cost-effective 3d transition metals and their alloys (TMs/TMAs) have demonstrated

* Corresponding authors.

E-mail addresses: talkhao@ustc.edu.cn (H. Tan), kongyuan@ustc.edu.cn (Y. Kong), haibohu@ahu.edu.cn (H. Hu).

¹ These authors contributed equally to this work.

significant potential as oxygen electrocatalysts. This is attributed to their rich and adjustable d-orbital electron structure, which greatly impacts the adsorption energy of oxygen-containing intermediates, leading to excellent oxygen electrocatalytic activity [24,25]. Nevertheless, the TMs/TMAs based bifunctional catalysts still face significant challenges. These include: (i) poor stability due to high reactivity in the strong corrosiveness of dominant alkaline electrolytes employed in ZABs, and (ii) insufficient activity for oxygen reduction reaction (ORR) resulting from poor oxygen binding energy and low selectivity towards the desired four-electron reduction pathway. These challenges greatly discourage their application [26,27]. Consequently, despite the comparable catalytic activity to noble metal-based catalysts and significant cost advantages, the enhancement of energy efficiency and cycle life in assembled full ZABs utilizing these cutting-edge TMs/TMAs based catalysts remains limited [28,29].

Construction of a protective armor to encapsulate the TMs/TMAs based catalysts, thus avoiding direct contact with strong alkaline electrolyte, has been proposed to be an effective scheme to enhance the durability of the obtained hybrid catalysts [30–32]. As an example, Bao's group encapsulated Fe nanoparticles into an armour-like carbon nanotube to physically isolate them from the harsh environments, and delivering a remarkably stable cell performance for more than 200 h [33]. In a similar vein, Miao et. al reported that an ultrathin P-doped carbon shell acted as a chainmail for Ni₂P, enabling electron penetration from the inner Ni₂P core. This characteristic led to the material exhibiting exceptional stability during rigorous electrochemical tests [34]. However, the introduction of protective layer would inevitably sacrifice the catalytic activity of the hybrid catalysts due to the shielding of partial active sites [35,36]. In addition, the existence of extra outer shell will block the transfer of ORR/oxygen evolution reaction (OER) related reactants at the multiphase interfaces in air cathode, thus further weakening the catalytic activity of the catalysts [35,36]. Moreover, the construction of most protective armor is not helpful to strengthen the inherently deficient ORR catalytic activity of the TMs/TMAs based catalysts [37,38]. Therefore, how to endow the armor with both high ORR and OER catalytic activity while preserving its protective function to encapsulate TMs/TMAs holds significant importance in advancing sustainable bifunctional electrocatalysts with a combination of high catalytic stability, activity, and cost-effectiveness for zinc-air batteries, but it is still challenging [39,40].

In this work, we present an innovative strategy for designing a multifunctional carbon armor to encapsulate the TMs/TMAs, aiming to achieve a combination of high catalytic activity and durability in the obtained cost-effective bifunctional hybrid catalysts. This strategy involves embedding Ni₃Fe nano-alloys within carbon nanotubes (CNTs) with abundant mesoporous defects and Fe-N₄ moieties (Ni₃Fe@CNTs/Fe-N₄) through an easily-manipulated two-step chemical vapor deposition process. The combination of density functional theory (DFT) calculation and in-situ synchrotron Fourier transform infrared (SR-FTIR) spectra/ex-situ synchrotron X-ray absorption spectra, revealed that the simultaneously enhanced ORR and OER catalytic activities could be attributed to two distinct factors. Specifically, the constructed Fe-N₄ moiety facilitated the ORR kinetics, while the introduced defective carbon atoms, rich in positive charges within the CNTs matrix near the embedded Ni₃Fe nano-alloys, promoted the OER kinetics. Consequently, the obtained Ni₃Fe@CNTs/Fe-N₄ hybrid catalyst not only manifests remarkable catalytic activity ($E_{1/2}=0.86$ V and $E_{1/10}=1.59$ V, 0.1 M KOH) but also demonstrates exceptional cyclic stability. In the 450-hour chronopotentiometry test, it maintains an 86.5% retention rate, whereas RuO₂ drops to 86.2% after 10 hours, which can be attributed to the stability provided by the multifunctional carbon armor. As a result, the further assembled ZABs based on Ni₃Fe@CNTs/Fe-N₄ hybrid bifunctional catalyst acquired a remarkable cycle life of over 300 hours and a high peak power density of 150 mW cm⁻². The demonstrated concept of constructing multifunctional carbon armor, capable of simultaneously enhancing oxygen catalytic reaction kinetics, multiphase mass transfer

dynamics, and the robustness of the hybrid air-cathode catalyst, contributes to the further development of practical ZABs with high energy efficiency and extended lifespan.

2. Experimental section

2.1. Materials

Iron (III) nitrate nonahydrate (Fe(NO₃)₃•9 H₂O, AR), nickel (II) nitrate hexahydrate (Ni(NO₃)₂•6 H₂O, AR), glucose (C₆H₁₂O₆, AR), zinc acetate (Zn(CH₃COO)₂, AR), potassium hydroxide (KOH, AR), acrylamide (C₃H₅NO, AR), acrylic acid (C₃H₄O₂, AR), N-N methylene bisacrylamide (C₇H₁₀N₂O₂, AR), ammonium persulfate ((NH₄)₂S₂O₈, AR) and carbon nanotubes (CNTs) were all purchased from Aladdin Scientific Corporation. Hydrazine hydrate (N₂H₄•H₂O, 80%) was purchased from Sigma-Aldrich. Nafion solution was purchased from Shanghai Macklin Biochemical Technology Co., Ltd. All reagents were analytical grade, and no further purification was required.

2.2. Preparation of acidified carbon cloth

Typically, a piece of hydrophilic carbon cloth (1 × 3 cm) was immersed into the solution of nitric acid and subsequently subjected to an oven at a temperature of 120 °C for a duration of 8 hours. Following this, the carbon cloth was thoroughly washed with water and alcohol for several times, and subsequently dried to yield acidified carbon cloth (CC-A).

2.3. Synthesis of N-doped graphene

Following our previously reported method [39], 5 g of dihydrodiamine (nitrogen source) and 0.25 g of glucose (carbon source) were dissolved in 100 ml of deionized water. The solution was subsequently dried in an oven at 80°C for 12 hours, resulting in the formation of a powdered precursor. The obtained powder was then mixed with CC-A (serving as a current collector for material growth) and heated in a tube oven at 900°C for 2 hours. After natural cooling, approximately 0.25 g of the target black powder sample was carefully scraped out from CC-A and designated as N-doped graphene (N-GN).

2.4. Synthesis of Fe-single-atom catalysts

25 mg of Fe(NO₃)₃•9 H₂O (iron source for Fe-N₄) was dissolved in 100 ml of deionized water, followed by the addition of 0.25 g of N-GN powder into the solution. After sonication for 2 h, the mixture was collected and dried in an oven for 2 h to obtain the powder precursor. Subsequently, the precursor was transferred to a tube furnace and annealed at 420°C under an Ar atmosphere for 2 h. Finally, the resulting powder (approximately 0.25 g) was named Fe-single-atom catalysts (Fe-SACs).

2.5. Synthesis of Ni₃Fe@CNTs

First, 5 g of dihydrodiamine, 0.25 g of glucose, 0.25 g of Ni(NO₃)₂•6 H₂O (nickel source for Ni₃Fe), 0.1 g of Fe(NO₃)₃•9 H₂O (iron source for Ni₃Fe) were dissolved in 100 ml of deionized water. The subsequent steps follow the same procedure as the method for preparing N-GN. The resulting powder (approximately 0.3 g) is named Ni₃Fe@CNTs.

2.6. Synthesis of Ni₃Fe@CNTs/Fe-N₄

25 mg of Fe(NO₃)₃•9 H₂O was dissolved in 100 ml of deionized water, followed by the addition of 0.25 g of Ni₃Fe@CNTs powder into the solution. After sonication for 2 h, the mixture was collected and dried in an oven for 2 h to obtain the powder precursor. Subsequently,

the precursor was transferred to a tube furnace and annealed at 420°C under an Ar atmosphere for 2 h. Finally, the resulting powder (approximately 0.3 g) was named Ni₃Fe@CNTs/Fe-N₄.

2.7. Synthesis of Ni₃Fe

According to the previously reported method [40], 1.04 g of nickel nitrate and 0.6 g of iron nitrate were simultaneously dissolved in 50 ml of deionized water to obtain solution A. Meanwhile, 2 g of NaOH was dissolved in 15 ml of N₂H₄·H₂O solution to obtain solution B. Subsequently, solution B was gradually added into solution A. After stirring for 20 minutes, the mixture was transferred to a 100 ml reaction vessel and subjected to a 2-hour reaction at 180 °C. Following this, the clear

liquid was decanted, leaving a black precipitate at the base of the reaction vessel. This precipitate was meticulously washed with deionized water and alcohol multiple times before being dried in a vacuum oven for 2 hours, resulting in the formation of black powder named Ni₃Fe.

2.8. Fabrication of liquid Zn-air batteries

First, the catalyst ink was prepared according to the aforementioned standard procedure. Subsequently, the catalyst ink was deposited onto a hydrophobic carbon paper for air cathode, ensuring a catalyst loading of 1.0 mg cm⁻². Zinc foil was employed as the anode, while the electrolyte was a 6 M KOH solution containing 0.2 M Zn(CH₃COO)₂. Finally, the liquid Zn-air battery was fabricated by assembling the air cathode with

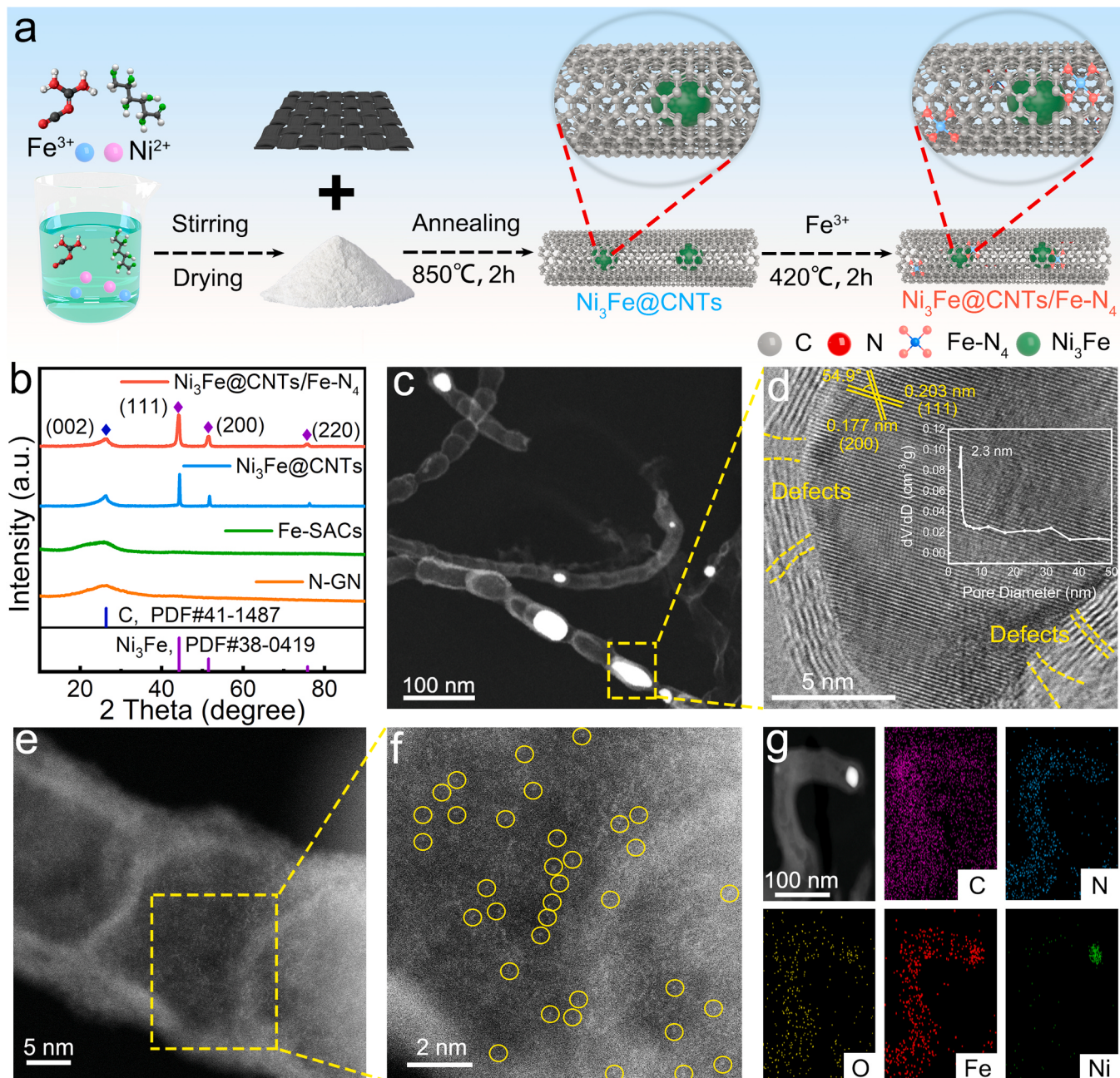


Fig. 1. a) Scheme illustration for the synthetic procedure of Ni₃Fe@CNTs/Fe-N₄. b) Comparison of XRD patterns of Ni₃Fe@CNTs/Fe-N₄ and the control samples. c) TEM and d) the corresponding localized HR-TEM images of Ni₃Fe@CNTs/Fe-N₄. Inset: pore size distribution curve. e) HAADF-STEM and f) the corresponding localized images of Ni₃Fe@CNTs/Fe-N₄ with the bright points representing iron single atoms. g) TEM image and the corresponding EDS mapping images of Ni₃Fe@CNTs/Fe-N₄.

catalyst, Zn anode, and the electrolyte into the home-made cell.

2.9. Synthesis of PAA-PAM/6 M KOH hydrogel

First, a mixture comprising 50 ml of deionized water, zinc acetate (0.2 mol/L), KOH (6 mol/L), 5 g of acrylamide (AM), and 5 ml of acrylic acid (AA) was meticulously blended using magnetic agitation. Subsequently, the solution was allowed to cool down to ambient temperature, following which 0.01 g of N-N methylene bisacrylamide was introduced. Nitrogen gas was continuously introduced for a duration of 15 minutes, and 0.1 g of ammonium persulfate was incorporated. Finally, the solution was treated in an oven at 80 °C for 3 hours, and the PAA-PAM/6 M KOH hydrogel was obtained.

2.10. The fabrication of flexible solid-state Zn-air batteries

First, a laser cutter was used to shape the 0.05 mm zinc foil and the hydrophobic carbon cloth into the required specifications. Subsequently, the previously prepared catalyst ink was coated onto the carbon cloth at a mass loading of 1 mg cm⁻² for flexible air cathode. Once the catalyst ink dried, the PAM-PAA/6 M KOH gel was coated onto the flexible air cathode. The paired Zn anode was then affixed onto the silicone package (Ecoflex 0030, with a mixing ratio of 1 A:1B by weight) using uncured silicone as the adhesive. Lastly, an all-solid-state rechargeable zinc-air battery was successfully fabricated by subjecting the battery to an oven at 60 °C for 20 minutes.

3. Results and discussion

3.1. Characterizations of the structure and composition of the catalysts

Fig. 1a presents the synthesis route and structural schematic diagram of the Ni₃Fe@CNTs/Fe-N₄ hybrid catalyst, which was synthesized via a two-step calcination method. First, the CNTs with abundant mesoporous defects and embedded Ni₃Fe binary nano-alloys were prepared by simply annealing the uniformly mixed precursor consisting of dicyandiamides, glucose, nickel and ferrous salts. Then, the Fe-N₄ moieties were further introduced into the CNTs matrix via a following pyrolysis procedure. The crystal structure and morphology of the obtained samples were comprehensively analyzed by scanning electron microscope (SEM), X-ray diffraction (XRD), transmission electron microscope (TEM) and high-angle annular dark field scanning transmission (HAADF). As observed from the SEM images (**Figure S1a, b, c**), a large number of CNTs grown on the surface of carbon cloth substrate, with a large number of nanoparticles uniformly encapsulated within the matrix. The coexistence of graphitic carbon and Ni₃Fe alloy phase in the sample can be further proved by the XRD patterns (**Fig. 1b**), which clearly demonstrate the characteristic peaks respectively belonging to the standard JCPDS#38-0491: Ni₃Fe and JCPDS#41-1487: C [41,42]. The further structural information of the sample was explored by TEM and High-resolution TEM (HRTEM) image, as shown in **Fig. 1c, d** and **Figure S2**. It's can be seen that the Ni₃Fe alloy nanoparticles were fully encapsulated by the carbon shell, and the lattice spacing of the Ni₃Fe alloy nanoparticles was found to be 2.04 Å and 1.77 Å, which is consistent with the crystallographic (111) plane and (200) plane of the Ni₃Fe crystalline phase [43]. Meanwhile, no particles were observed on the outer shells of CNTs when scanning randomly across the sample under the electron microscope. Most notably, numerous mesoporous defects are present on the surface of the CNTs matrix, as highlighted in **Fig. 1d** with yellow dashed lines. The fact is further confirmed by detailed analysis of Raman spectrum and the pore size distribution curve. For the Ni₃Fe@CNTs/Fe-N₄ catalyst, the intensity ratio of the D-band (defect-induced peak) to the G-band in the Raman spectrum is larger than that of other comparative sample, indicating the presence of more defect structures (**Figure S3**) [44]. Additionally, observation of the pore size distribution curve (inset in **Fig. 1d**) reveals the existence of rich

mesopores with an average pore diameter of approximately 2.3 nm. These abundant mesopores are the fundamental reason for the exhibited high degree of defectiveness and the large specific surface area (705.65 m² g⁻¹) of the Ni₃Fe@CNTs/Fe-N₄ catalyst (**Figure S4**). We envisaged that these abundant mesoporous defects could act as channels to facilitate the ORR/OER related mass transfer during the catalytic reactions. Subsequently, in order to directly observe the dispersion of Fe atoms on the CNTs at the atomic scale, the aberration-corrected high-angle annular dark-field scanning transmission electron microscopy (HAADF-STEM) was carried out (**Fig. 1e**). As shown in **Fig. 1f**, a large number of bright dots can be seen in the CNTs, indicating that Fe atoms are isolated distribution in CNTs. Additionally, the Energy-dispersive X-ray spectroscopy (EDS) mapping (**Fig. 1g**) reveals Ni atoms are mainly distributed in the packaged nanoparticles, existing in the form of alloy combined with Fe atoms, while a large number of isolated Fe single atoms were evenly distributed in the CNTs matrix. Meanwhile, the percentage of elemental content in the Ni₃Fe@CNTs/Fe-N₄ is shown in **Figure S5**. These results prove that we have successfully fabricated a protective CNTs that serve as the chainmail to encapsulate the Ni₃Fe nano-alloys, of which the matrix simultaneously have massive Fe single atoms for additional catalytic active site and mesoporous defects to promote mass transfer.

3.2. Spectra analysis on the catalysts

In order to accurately reveal the chemical state and coordination environment of the Ni and Fe species in the Ni₃Fe@CNTs/Fe-N₄ hybrid and control samples, the synchrotron X-rayabsorption spectroscopy (XAS) and X-ray photoelectron spectroscopy (XPS) were further carried out. In the Ni X-ray absorption near-edge structure (XANES), the absorption edge of the Ni₃Fe@CNTs/Fe-N₄ almost coincides with that of pure Ni foil, indicating that the valent state of existent Ni specie is close to 0 (**Figure S6**) [44,45]. Meanwhile, the XANES spectrum of Ni₃Fe@CNTs overlaps with that of pure Fe foil, while the spectrum of Ni₃Fe@CNTs/Fe-N₄ shows an E_0 shift towards higher energy (**Fig. 2a**). The phenomenon demonstrates that the average valence state of the Fe species in the Ni₃Fe@CNTs/Fe-N₄ sample has increased due to the coexistence of single Fe atoms in coordination with other elements within the CNTs matrix [46]. The coordination environment of the single Fe atoms within the CNTs matrix could be revealed by the XPS and N K-edge XANES. From the N 1 s XPS spectra (**Figure S7**), the peak at 399.7 eV corresponding to the Fe-N bond could be observed [47]. And, the N K-edge spectra (**Fig. 2b**) of Ni₃Fe@CNTs/Fe-N₄ and Fe-SACs display a key characteristic peak at 399 eV, which can be assigned to the transition of N 1 s core electrons into hybridized states between N 2p and Fe 3d, further demonstrating the formation of Fe-N bonds in Ni₃Fe@CNTs/Fe-N₄ [48]. The Fourier-transformed EXAFS (FT-EXAFS) spectra of Fe K-edge for Ni₃Fe@CNTs/Fe-N₄ further indicates the coexistence of Fe-N and metallic Fe-Fe/Ni scattering paths at ~1.6 Å and 2.2 Å (without phase correction), respectively (**Fig. 2c**), whereas for Ni FT-EXAFS spectra, only a dominant peak at ~2.2 Å, which is ascribed to the first shell of Ni-Ni/Fe (**Fig. 2d**), was observed [22,23,49–51]. The Fe and Ni K-edge wavelet transform (WT)-EXAFS was also applied to investigate the atomic configuration of Ni₃Fe@CNTs/Fe-N₄. The WT-EXAFS of Fe is shown in **Fig. 2e**, and Fe-N and Fe-Fe/Ni bonds are also observed. Moreover, the least-squares EXAFS fitting results (**Fig. 2f** and **Table S1, 2**) show that the average coordination number of the Ni-Ni/Fe and Fe-Fe/Ni in the Ni₃Fe@CNTs/Fe-N₄ are 8.7 and 8.9, respectively, which were lower than the value of metal foil (12). This is due to the increase of unsaturated coordination bonds on the surface of Ni₃Fe nano-alloys [52]. Additionally, the average coordination number of single Fe atoms was ~4.2 with a bond length of 2.0 Å (**Table S1, 2**), suggesting that atomically dispersed Fe atoms exist in Ni₃Fe@CNTs-/Fe-N₄ hybrid in the form of Fe-N₄ moieties (**Fig. 2g**). These results further verify that the coexistence of Ni₃Fe nano-alloys and the atomically dispersed Fe-N₄ active sites in the Ni₃Fe@CNTs/Fe-N₄ sample.

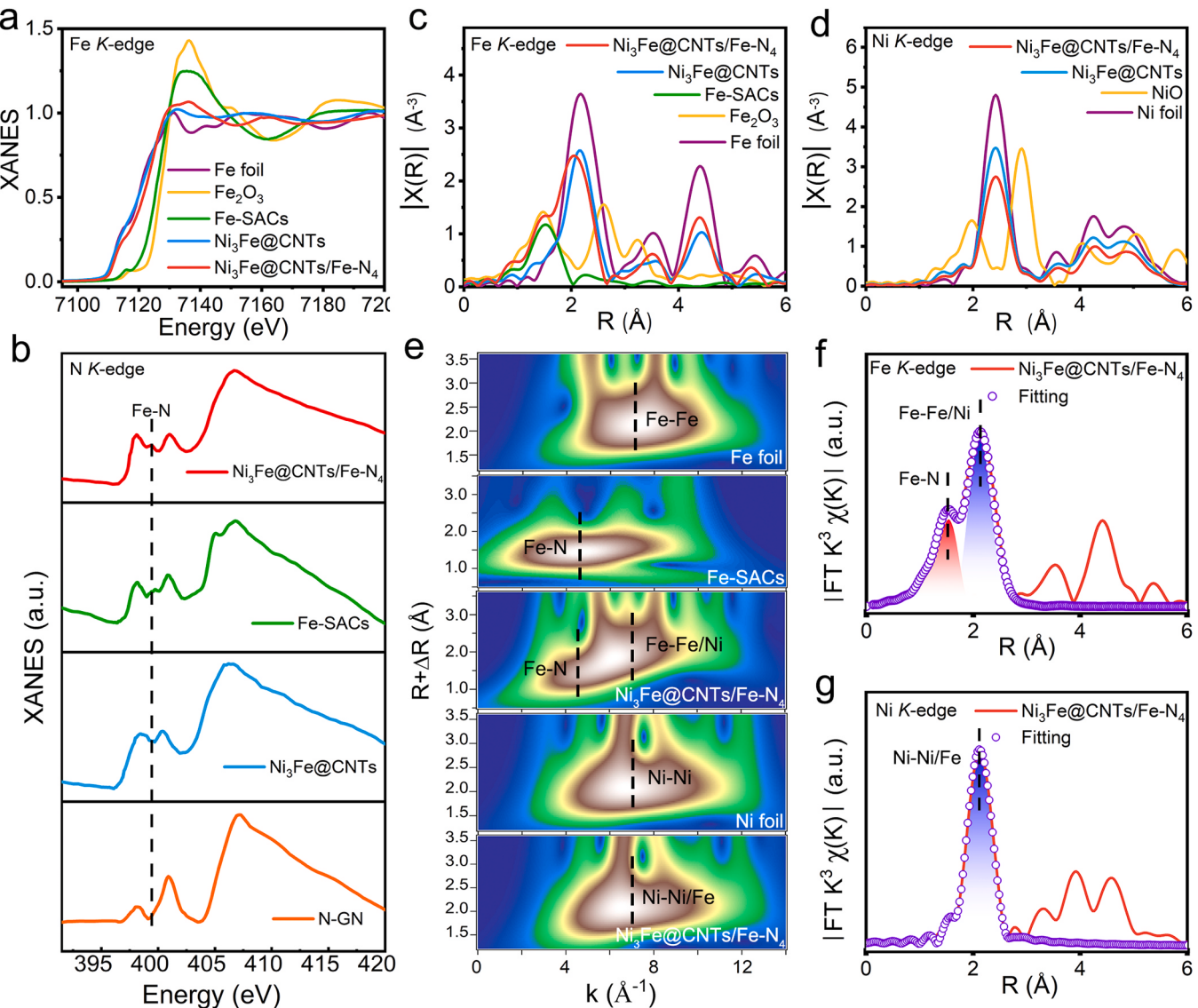


Fig. 2. a) Fe K-edge XANES. b) N K-edge XANES spectra of $\text{Ni}_3\text{Fe}@\text{CNTs}/\text{Fe}-\text{N}_4$, $\text{Ni}_3\text{Fe}@\text{CNTs}$, Fe-SACs and N-GN. FT-EXAFS curves of $\text{Ni}_3\text{Fe}@\text{CNTs}/\text{Fe}-\text{N}_4$, $\text{Ni}_3\text{Fe}@\text{CNTs}$, Fe-SACs and reference materials at c) Fe K-edge and d) Ni K-edge. e) Wavelet transform of Fe and Ni K-edge EXAFS for $\text{Ni}_3\text{Fe}@\text{CNTs}/\text{Fe}-\text{N}_4$ and references. f) Fe and g) Ni K-edge EXAFS fitting curves of $\text{Ni}_3\text{Fe}@\text{CNTs}/\text{Fe}-\text{N}_4$ in R-space.

3.3. Catalytic performance evaluation of the catalysts

The electrochemical ORR performance of the well-designed $\text{Ni}_3\text{Fe}@\text{CNTs}/\text{Fe}-\text{N}_4$ electrocatalyst was first evaluated by using a rotating disk electrode (RDE) in oxygen-saturated 0.1 M KOH electrolyte, together with the $\text{Ni}_3\text{Fe}@\text{CNTs}$, Fe-SACs, N-GN and Pt/C as comparsons. All the potentials were calibrated to the reversible hydrogen electrode (RHE). As seen in the cyclic voltammetry (CV) curves (Figure S8), the $\text{Ni}_3\text{Fe}@\text{CNTs}/\text{Fe}-\text{N}_4$ exhibits a well-defined cathodic peak at 0.84 V, while the $\text{Ni}_3\text{Fe}@\text{CNTs}$ has a much lower peak (0.65 V), indicating the significant role of the introduced $\text{Fe}-\text{N}_4$ moieties in enhancing the ORR kinetics of the $\text{Ni}_3\text{Fe}@\text{CNTs}/\text{Fe}-\text{N}_4$ hybrid catalyst. In addition, $\text{Ni}_3\text{Fe}@\text{CNTs}/\text{Fe}-\text{N}_4$ exhibited the highest half-wave potential ($E_{1/2}=0.86$ V, Fig. 3a) compared to that of commercial Pt/C (0.83 V), Fe-SACs (0.80 V) and $\text{Ni}_3\text{Fe}@\text{CNTs}$ (0.77 V), proving the best ORR performance. Even compared to state-of-the-art catalysts recently reported, its ORR performance still remains highly competitive (Table S3). The highest ORR catalytic activity of $\text{Ni}_3\text{Fe}@\text{CNTs}/\text{Fe}-\text{N}_4$ is also evidenced by its smallest Tafel slope (92 mV dec⁻¹) relative to that of Fe-SACs (113 mV dec⁻¹) and $\text{Ni}_3\text{Fe}@\text{CNTs}$ (119 mV dec⁻¹) (Fig. 3b).

[53]. In contrast to the control sample, $\text{Ni}_3\text{Fe}@\text{CNTs}/\text{Fe}-\text{N}_4$ demonstrates superior mass transfer efficiency, showcasing the swiftest kinetics (Figure S9). Furthermore, increasing the electrode rotation speed leads to a proportional increase in current density (Figure S10), indicating the first-order oxygen reduction reaction. These results further prove that the $\text{Fe}-\text{N}_4$ sites are the major active centers for the enhanced ORR kinetics. Moreover, the calculated number of transferred electrons of $\text{Ni}_3\text{Fe}@\text{CNTs}/\text{Fe}-\text{N}_4$ is close to 4, and the hydrogen peroxide yield was less than 5% (Fig. 3c), suggesting that $\text{Ni}_3\text{Fe}@\text{CNTs}/\text{Fe}-\text{N}_4$ catalyzes the ORR through a direct four-electrons pathway [54]. Not only with the prominent ORR performance, the $\text{Ni}_3\text{Fe}@\text{CNTs}/\text{Fe}-\text{N}_4$ also exhibits high activity for OER.

As shown in Fig. 3d, the overpotential of $\text{Ni}_3\text{Fe}@\text{CNTs}/\text{Fe}-\text{N}_4$ to reach 10 mA cm⁻² is only 360 mV, which far surpasses that of the Fe-SACs (470 mV), $\text{Ni}_3\text{Fe}@\text{CNTs}$ (395 mV), and benchmark catalyst of RuO₂ (400 mV), respectively. The facilitated OER kinetics could be attributed to the synergistic effect of the defect carbon around the encapsulated Ni_3Fe nanoparticles and the Fe-SACs. To elucidate the distinct contributions of each component in the ORR and OER process, defect-rich carbon nanotubes (D-CNTs) were further synthesized via

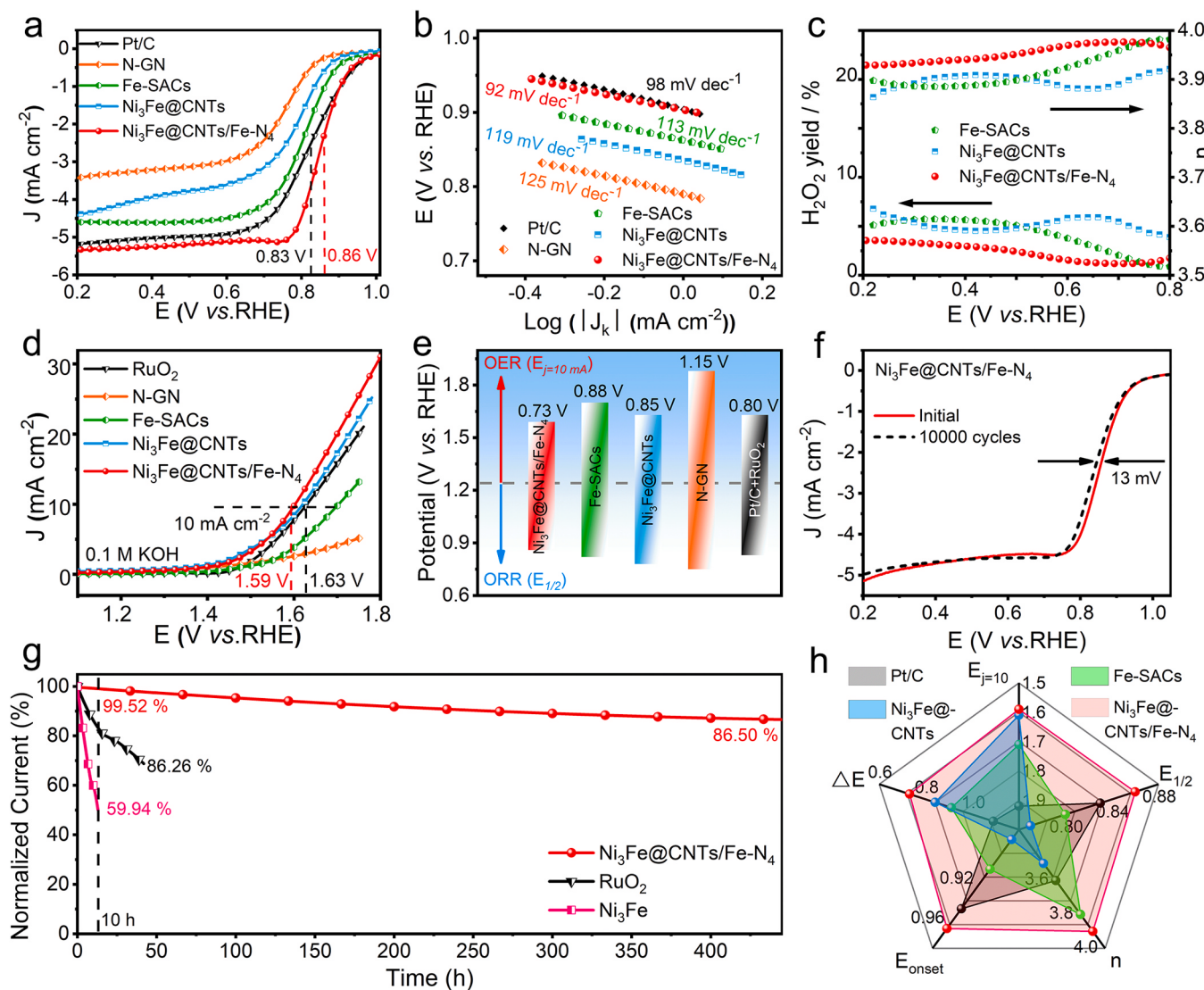


Fig. 3. a) ORR polarization profiles of the $\text{Ni}_3\text{Fe}@\text{CNTs}/\text{Fe-N}_4$, $\text{Ni}_3\text{Fe}@\text{CNTs}$, Fe-SACs, N-GN and Pt/C in O_2 -saturated 0.1 M KOH solution. b) The corresponding Tafel plots. c) Peroxide yield and electron transfer number for the samples based on RRDE voltammograms at a rotating speed of 1600 rpm in O_2 -saturated 0.1 M KOH . d) LSV curves of the samples in 0.1 M KOH solution for OER. e) Comparison of different catalysts in ORR/OER bifunctional electrocatalytic performance. f) Cyclic stability testing of LSV curves on ORR performance. g) Long-time stability test of the catalyst at a constant current density of 10 mA cm^{-2} . h) Radar plot for evaluating each of the catalyst's metrics.

plasma treatment of carbon nanotubes [56]. Then, the Fe-N₄ species were introduced into the obtained D-CNTs matrix using the same method employed for synthesizing the Fe-single-atom catalyst, resulting in Fe-D-CNTs for comparative analysis (Figure S11, 12). Following this, the ORR and OER performances of D-CNTs, Fe-D-CNTs, and $\text{Ni}_3\text{Fe}@\text{CNTs}/\text{Fe-N}_4$ were evaluated. Experimental findings indicate a significant enhancement in the ORR performance of both Fe-D-CNTs and $\text{Ni}_3\text{Fe}@\text{CNTs}/\text{Fe-N}_4$ catalysts with the presence of the Fe-N₄ structure, compared to D-CNTs without Fe-N₄ species (Figure S13). Moreover, in contrast to the $\text{Ni}_3\text{Fe}@\text{CNTs}/\text{Fe-N}_4$ sample, both D-CNTs (containing only defects) and Fe-D-CNTs (possessing defects and Fe-N₄ species) exhibited inferior performance in the OER process (Figure S13). This underscores the pivotal role of Ni_3Fe alloy nanoparticles in enhancing OER efficiency. To comprehensively evaluate the bifunctional catalytic activity of $\text{Ni}_3\text{Fe}@\text{CNTs}/\text{Fe-N}_4$, the potential difference (ΔE) between $E_{1/2}$ for ORR and $E_{j=10}$ for OER was summarized and compared with that of the control samples. As shown in Fig. 3e and Figure S14, the $\text{Ni}_3\text{Fe}@\text{CNTs}/\text{Fe-N}_4$ owns the lowest ΔE of 0.73 V relative to the other counterparts (Fe-SACs, 0.88 V ; $\text{Ni}_3\text{Fe}@\text{CNTs}$, 0.85 V ; N-GN, 1.15 V ;

Pt/C+RuO₂, 0.80 V), indicating its superior bifunctional catalytic performance, which can be attributed to the significantly improved oxygen reaction kinetics rooting in the innovative multifunctional carbon armor design.

The synchronously enhanced electrochemical durability of the $\text{Ni}_3\text{Fe}@\text{CNTs}/\text{Fe-N}_4$ was further verified by the accelerated durability test (ADT) and chronoamperometry test. The experimental results revealed a negligible decay of only 13 mV for $E_{1/2}$ after $10,000$ continuous cycles (Fig. 3f). Additionally, to further corroborate the protective effect of the carbon armor, Ni_3Fe alloy without armor was prepared for comparison (Figure S15). As depicted in Fig. 3g, the stability of the Ni_3Fe alloy decreased to 59.4% after 10 hours. However, owing to the protection provided by the carbon armor, the $\text{Ni}_3\text{Fe}@\text{CNTs}/\text{Fe-N}_4$ catalyst demonstrated an impressive current retention of 99.52% during the 10 -hour continuous chronoamperometry test at 1.59 V , which remained as high as 86.50% even after 450 hours. This performance significantly outperformed the current retention of Pt/C+RuO₂ catalyst, validating the superior stability of $\text{Ni}_3\text{Fe}@\text{CNTs}/\text{Fe-N}_4$ compared to the benchmark mixed catalyst in long-term

electrochemical processes. The results also indicate that under alkaline conditions, both the catalytic activity (for ORR and OER) and stability of $\text{Ni}_3\text{Fe}@\text{CNTs}/\text{Fe-N}_4$ surpass those of the commercial Pt/C and RuO₂ catalysts. To further substantiate the impact of this "multifunctional armor" on catalyst stability, we conducted a comparative analysis of the stability of recently reported bifunctional catalysts (ORR and OER). The results demonstrate that, in alkaline environments, the $\text{Ni}_3\text{Fe}@\text{CNTs}/\text{Fe-N}_4$ catalyst exhibits the longest stability duration and the slowest rate of stability degradation per unit time, rivaling the highest-level stability reported in recent years (Figure S16). Finally, a radar map summarizing the performance indicators of the $\text{Ni}_3\text{Fe}@\text{CNTs}/\text{Fe-N}_4$ and the control samples was plotted (Fig. 3h). As depicted in the radar plot, it can be concluded that the $\text{Ni}_3\text{Fe}@\text{CNTs}/\text{Fe-N}_4$ exhibits significant advantages in all performance indicators, confirming the outstanding catalytic performance.

3.4. Full Zn-air battery performance evaluation

Given the excellent bifunctional activity of the designed $\text{Ni}_3\text{Fe}@\text{CNTs}/\text{Fe-N}_4$ hybrid catalyst, the full ZAB was further assembled and the corresponding energy efficiency was evaluated. As shown in Fig. 4a, the schematic diagram illustrates the basic configuration of the

assembled full ZAB, wherein the entire device consists of a zinc foil as the anode, a hydrophobic carbon cloth loaded with $\text{Ni}_3\text{Fe}@\text{CNTs}/\text{Fe-N}_4$ hybrid catalyst as the cathode, and a 6 M KOH/0.2 M $\text{Zn}(\text{OAc})_2$ mixed solution serving as the electrolyte. Reference ZAB was also assembled by using commercial Pt/C+RuO₂ catalyst for air cathodes. As shown in Fig. 4b, c, d, the $\text{Ni}_3\text{Fe}@\text{CNTs}/\text{Fe-N}_4$ based ZAB delivered a larger open circuit potential (OCP) of 1.43 V, a higher capacity of 797.4 mAh g⁻¹, and a higher peak power density of 150 mW cm⁻² than the values of ZAB assembled with the benchmark Pt/C+RuO₂ mixed catalysts (1.40 V, 717.1 mAh g⁻¹, 106 mW cm⁻²), suggesting the promising potential of $\text{Ni}_3\text{Fe}@\text{CNTs}/\text{Fe-N}_4$ in practical application. In addition, compared to the cell employing the commercial Pt/C+RuO₂ mixed catalysts, the $\text{Ni}_3\text{Fe}@\text{CNTs}/\text{Fe-N}_4$ based ZAB delivered higher discharge voltages under different current densities (Fig. 4e). Even at a current density of 10 mA cm⁻², the cell utilizing $\text{Ni}_3\text{Fe}@\text{CNTs}/\text{Fe-N}_4$ catalyst acquired a high dicharge voltage of 1.21 V, exceeding that (1.19 V) based on Pt/C+RuO₂ mixed catalysts. Moreover, a light-emitting diode (LED) scroller with a ZAB signal could be lighted by the three series-connected $\text{Ni}_3\text{Fe}@\text{CNTs}/\text{Fe-N}_4$ based ZABs, confirming the feasibility of the $\text{Ni}_3\text{Fe}@\text{CNTs}/\text{Fe-N}_4$ catalyst in practical applications (Fig. 4f). The cyclic stability of the zinc-air battery assembled with different catalysts was subsequently evaluated through constant-current discharge-

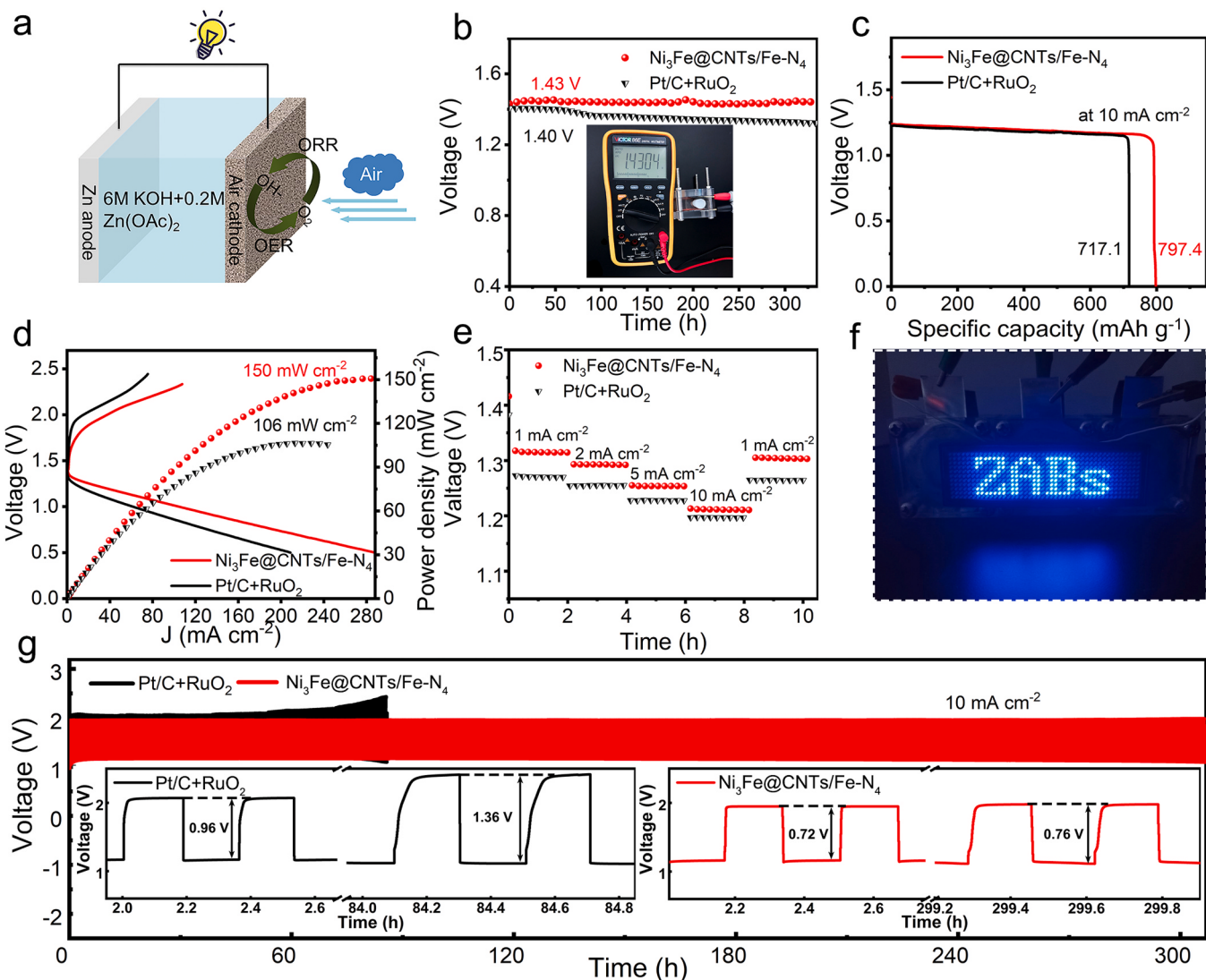


Fig. 4. a) A schematic configuration of the full Zinc-air battery. Comparison of b) the open-circuit voltages, c) power densities, d) capacities and e) rate performance. f) Photograph of a blue LED screen powered by three Zinc-air batteries in series connection, with carbon cloth loaded with $\text{Ni}_3\text{Fe}@\text{CNTs}/\text{Fe-N}_4$ catalyst serving as the air cathode. g) cycle stabilities of the assembled Zinc-air batteries respectively based on $\text{Ni}_3\text{Fe}@\text{CNTs}/\text{Fe-N}_4$ and Pt/C+RuO₂ mixed catalysts.

charge cycling tests at a fixed current density of 10 mA cm^{-2} . Clearly, compared to its counterpart based on Pt/C+RuO₂, the zinc-air battery based on Ni₃Fe@CNTs/Fe-N₄ exhibited a higher and narrower voltage window (from 0.72 V to 0.76 V) that could be maintained over a longer cycling time of 307 hours. In contrast, the voltage window of the zinc-air battery based on Pt/C+RuO₂ started to widen rapidly, increasing from 0.96 V to 1.36 V after only 84 hours of cycling (Figure 4g). Benefiting from the excellent charge-discharge performance of the battery and the catalyst's high catalytic activity and exceptional stability at the air cathode, this ZAB achieves a groundbreaking level of performance. In comparison to the recently reported state-of-the-art ZABs, Ni₃Fe@CNTs/Fe-N₄-based ZABs also exhibit strong competitiveness in energy efficiency, as shown in Table S4 in the Supporting Information. Furthermore, the Ni₃Fe@CNTs/Fe-N₄ catalyst was further employed to fabricate a flexible solid zinc-air battery (FS-ZAB) (Figure S17a), which also acquired a long cycle life of 40 h (2 mA cm^{-2} , Figure S17b) and a high power density of 73 mW cm^{-2} (Figure S17c). These results suggest the higher stability and activity of Ni₃Fe@CNTs/Fe-N₄ than Pt/C+RuO₂ benchmark mixed catalysts.

3.5. Analysis on the catalytic mechanism of the Ni₃Fe@CNTs/Fe-N₄ hybrid catalyst

To gain an in-depth insight into the synergistic effects of the defect carbon around the encapsulated Ni₃Fe nanoalloys and the Fe-N₄ sites, which could play a vital role in enhancing the catalytic activity of Ni₃Fe@CNTs/Fe-N₄ for ORR and OER, the DFT calculations and SR-FTIR were further performed. The above experimental results have revealed there are a large number of carbon defects and single Fe-N₄ sites within the carbon nanotubes matrix. Given this, we first established four DFT calculation models based on the different coupling methods between the defect graphene and Ni₃Fe nanoparticle (Figure S18 and Table S5). Subsequently, we selected the best optimized model (Ni₃Fe@CNTs-A, Table S7) among them and built three possible structure models for introduction of the Fe-N₄ active sites into the defected graphene. The computational details are given in the supporting information (Figure S19). In addition, the Fe-SACs (Figure S20) were also added for comparison. The calculated results in Table S6 suggested that the model I of the Ni₃Fe@CNTs/Fe-N₄, in which the Fe-N₄ sites is close to the Fe atoms in Ni₃Fe, is the most stable model. The charge density distribution of Ni₃Fe@CNTs and Ni₃Fe@CNTs/Fe-N₄ are given in Figure S21, it is observed that the three C atoms surrounding the C defect are in closer proximity to the Ni₃Fe nanoparticle and could form the Fe-C bond, and

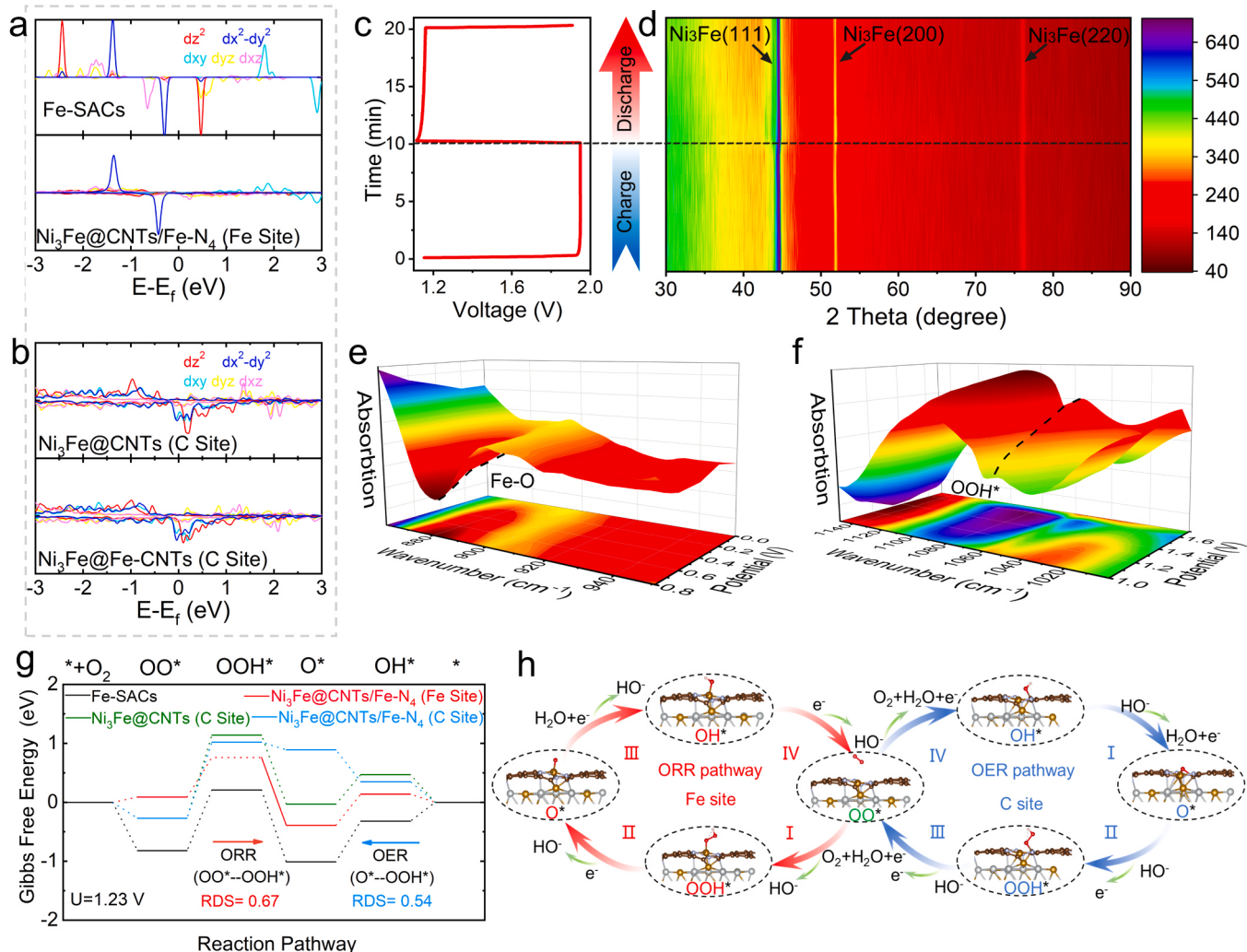


Fig. 5. a) PDOS for Fe-SACs and Ni₃Fe@CNTs/Fe-N₄ (Fe site). b) PDOS for Ni₃Fe@CNTs and Ni₃Fe@CNTs/Fe-N₄ (C site). c) The charge/discharge curves of the Ni₃Fe@CNTs/Fe-N₄ based ZAB. d) In-situ XRD pattern and e, f) Operando SR-FTIR spectra of Ni₃Fe@CNTs/Fe-N₄. g) Free energy diagrams at 1.23 V for ORR and OER over four types of active sites of Fe-SACs, Ni₃Fe@CNTs (C site), Ni₃Fe@CNTs/Fe-N₄ (Fe site) and Ni₃Fe@CNTs/Fe-N₄ (C site). h) Schematic for OER/ORR pathways of Ni₃Fe@CNTs/Fe-N₄. The spheres in gold, white, brown, red and pink denote the Fe, Ni, C, O and H atoms, respectively.

thus the distinctive electronic properties of these C atoms could potentially serve as the active site for OER. After introduction of the Fe-N₄ sites into the graphene, the electrons tend to transfer from Ni₃Fe nanoparticles to Fe-N₄ sites, suggesting the strong electronic coupling between the Ni₃Fe nano-alloys and the Fe-N₄ sites of the graphene, which is consistent with the results from XANES and XPS characterization. As a result, the introduced Fe-N₄ sites will activate the catalytic activity of carbon armor and potentially serve as the active sites for ORR.

Fig. 5a present the calculated projected density of states (PDOS) of the Fe sites in the carbon matrix, which showed that the increased electron occupation near Fermi surface in Ni₃Fe@CNTs/Fe-N₄, implying a weakened affinity for oxygen-containing intermediates. Compared with Ni₃Fe@CNTs, the C center's partial density of states (PDOS) in Ni₃Fe@CNTs/Fe-N₄ showed a negative shift (**Fig. 5b**). Higher electronic states neighboring the Fermi level were achieved on Ni₃Fe@CNTs/Fe-N₄, suggesting higher reactivity and electron mobility[55]. The in-situ XRD measurements were further carried out to track the chemical composition change of the Ni₃Fe@CNTs/Fe-N₄ hybrid catalyst during the ORR and OER processes, thus evaluating its stability. As shown in **Fig. 5c, d**, the characteristic peak belonging to the Ni₃Fe nano-alloys in the catalyst remained unchanged throughout the charge-discharge cycle of the full ZAB, directly indicating that the CNTs armor could effectively protect the Ni₃Fe nano-alloys from being corroded under the harsh reaction condition [56]. A similar conclusion can be drawn by comparing the state of the Ni₃Fe@CNTs/Fe-N₄ catalyst before and after the reaction of ORR and OER using XPS (**Figure S22**). Furthermore, the in-situ SR-FTIR spectra was used to explore the reaction mechanism of the Ni₃Fe@CNTs/Fe-N₄ hybrid catalyst for OER and ORR. During the ORR process (**Fig. 5e**), when the applied potential increased from 0 to 0.8 V, a new peak at $\sim 875\text{ cm}^{-1}$ which could be attributed to the Fe-O vibration of OOH* [57–59]. In order to determine whether the Fe-O vibration originated from the Fe-N₄ or the Ni₃Fe site, in-situ infrared spectroscopy tests were carried out on the Ni₃Fe@CNTs catalyst. The results showed the absence of Fe-O vibration during the ORR process, suggesting that the active site responsible for ORR is indeed the Fe-N₄ site (**Figure S23**). Meanwhile, a significant characteristic peak corresponding to the O-O bond vibration of OOH* can be clearly observed during the OER process (**Fig. 5f**), suggesting that the Ni₃Fe@CNTs/Fe-N₄ catalyst undergone a typical four-electrons associative OER pathway that proceeds through OH*, O*, OOH*, and O₂* [60–62]. Then, we calculated Gibbs free energy (ΔG) of Ni₃Fe@CNTs/Fe-N₄ for OER and ORR (**Fig. 5g**). In the case of the Ni₃Fe@CNTs (**Figure S24**), the ORR and OER take place at the C site next to the defect, with the transition from OO* to OOH* (1.41 eV) and from O* to OOH* (1.17 eV) being the rate-determining steps (RDS) for ORR and OER, respectively (**Figure S25b** and **Table S7, 8**). For the Ni₃Fe@CNTs/Fe-N₄ (**Figure S26**), the active sites for ORR shift from the C-site to the Fe-site (**Figure S25c**), resulting in a significant reduction of the energy barrier for the RDS by 0.67 eV (**Table S7**). Besides, the active sites for OER in the Ni₃Fe@CNTs/Fe-N₄ remain at the C sites (**Figure S25d**), and the synergistic effect between the Fe-N₄ sites and the Ni₃Fe nano-alloys helps to further reduce the energy barrier of the RDS of OER (1.17 eV to 0.54 eV, O* to OOH*) (**Figure S26** and **Table S8**). The detailed pathways of reversible OER/ORR reactions are summarized in **Fig. 5h**. The experimental results together with the theoretical simulations fully confirm that the introduction of the catalytic active carbon armor not only can effectively alleviate the corrosion of the encapsulated binary alloy nanoparticles during long-term service in harsh reaction conditions, but also would be a new design platform for further improving the catalytic performance, thus enabling fabrication of hybrid catalysts with both high activity and stability for ZABs with high energy efficiency and lifespan.

4. Conclusions

In summary, we proposed a strategy of fabricating a multifunctional armor for the transition-metal nano-alloys for designing highly durable

and bifunctional active nonprecious-metal catalysts. Experimentally, we encapsulated Ni₃Fe nano-alloys within Fe-N₄ moiety-doped porous carbon nanotubes. A series of ex-situ and in-situ experimental findings indicate strong electronic coupling between Ni₃Fe nanoparticles and Fe-N₄ moiety-doped CNTs. This coupling enables Ni₃Fe@CNTs/Fe-N₄ to exhibit excellent bifunctional activity, with a half-wave potential of 0.86 V for ORR and a potential of 1.59 V (in 0.1 M KOH) required to achieve 10 mA cm⁻² for OER. The preeminent bifunctionality is validated in a ZABs with a high efficiency of 59% and a long-term durability over 307 h, significantly superior than those of the benchmark cathode based on Pt/C+RuO₂. The in-situ SR-FTIR and DFT calculations reveal that Fe-N₄ moiety and carbon atoms next to the defect are served as the active sites for ORR and OER respectively. And the catalytic activity arises from the electron transfer from Ni₃Fe nano-alloys to the Fe-N₄ moiety doped CNTs leading to an optimization of the adsorption/desorption of the reaction intermediates. These findings provide a new concept for the rational design of chainmail catalysts for electrochemical applications.

CRediT authorship contribution statement

Lei Zhang: Writing – review & editing, Writing – original draft, Visualization, Validation, Software, Methodology, Investigation, Formal analysis, Data curation, Conceptualization. **He Jiang:** Methodology, Investigation, Software, Formal analysis, Data curation. **Yuan Kong:** Validation, Software, Project administration, Methodology, Funding acquisition, Conceptualization. **Haibo Hu:** Writing – review & editing, Supervision, Resources, Project administration, Methodology, Formal analysis. **Min Tang:** Visualization, Software, Resources. **Ying Jiang:** Resources, Formal analysis. **Bing Tang:** Validation, Methodology, Conceptualization. **Hao Tan:** Writing – review & editing, Validation, Supervision, Software, Resources, Formal analysis.

Declaration of Competing Interest

The authors declare that they have no known competing financial interests or personal relationships that could have appeared to influence the work reported in this paper.

Data Availability

Data will be made available on request.

Acknowledgements

This work was financed by National Natural Science Foundation of China (51871001), Excellent Youth Fund of Anhui Province (2108085Y17), Hundred-Talent Program of Anhui Province, Innovation and Entrepreneurship Support Plan of Anhui Province for Returned Personnels Studying Abroad (2022LCX001), Project supported by the Program of State Key Laboratory of Quantum Optics and Quantum Optics Devices (KF202212), Collaborative Innovation Program of Hefei Science Center, CAS (2022HSC-CIP028), Opening Foundation of Shanxi Provincial Key Laboratory for High Performance Battery Materials and Devices (2023HPBMD01001), and National Key Research and Development Program of China (2021YFA1200103). We thank the staff at SSRF beamline BL17B1 of the National Facility for Protein Science in Shanghai (NFPS), Shanghai Advanced Research Institute, CAS, for providing technical support in X-ray absorption fine Structure data collection and analysis

Appendix A. Supporting information

Supplementary data associated with this article can be found in the online version at doi:10.1016/j.apcatb.2024.124151.

References

- [1] Y. Li, H. Dai, Recent advances in zinc-air batteries, *Chem. Soc. Rev.* 43 (2014) 5257–5275.
- [2] J. Fu, Z.P. Cano, M.G. Park, A.P. Yu, M. Fowler, Z.W. Chen, Electrically rechargeable zinc-air batteries: progress, challenges, and perspectives, *Adv. Mater.* 29 (2017) 1604685.
- [3] J. Pan, Y.Y. Xu, H. Yang, Z. Dong, H. Liu, B.Y. Xia, Advanced architectures and relatives of air electrodes in Zn-Air batteries, *Adv. Sci.* 5 (2018) 1700691.
- [4] P. Gu, M. Zheng, Q. Zhao, X. Xiao, H. Xue, H. Pang, Rechargeable zinc-air batteries: a promising way to green energy, *J. Mater. Chem. A* 5 (2017) 7651–7666.
- [5] W. Sun, F. Wang, B. Zhang, M. Zhang, V. Kuepers, X. Ji, C. Theile, P. Bieker, K. Xu, C. Wang, M. Winter, A rechargeable zinc-air battery based on zinc peroxide chemistry, *Science* 371 (2021) 46–51.
- [6] L. An, Z. Zhang, J. Feng, F. Lv, Y. Li, R. Wang, M. Lu, R.B. Gupta, P. Xi, S. Zhang, Heterostructure-promoted oxygen electrocatalysis enables rechargeable zinc-air battery with neutral aqueous electrolyte, *J. Am. Chem. Soc.* 140 (2018) 17624–17631.
- [7] Y. Yan, S. Liang, X. Wang, M.Y. Zhang, S.M. Hao, X. Cui, Z.W. Li, Z.Q. Lin, Robust wrinkled MoS₂/N-C bifunctional electrocatalysts interfaced with single Fe atoms for wearable zinc-air batteries, *Proc. Natl. Acad. Sci. U. S. A.* 118 (40) (2021) e2110036118.
- [8] H. Niu, C. Xia, L. Huang, S. Zaman, T. Maiyalagan, W. Guo, B. You, B.Y. Xia, Rational design and synthesis of one-dimensional platinum-based nanostructures for oxygen-reduction electrocatalysis, *Chin. J. Catal.* 43 (2022) 1459–1472.
- [9] P. Tan, B. Chen, H. Xu, H. Zhang, W. Cai, M. Ni, M. Liu, Z. Shao, Flexible Zn- and Li-air batteries: recent advances, challenges, and future perspectives, *Energy Environ. Sci.* 10 (2017) 2056–2080.
- [10] H.F. Wang, C. Tang, Q. Zhang, A Review of Precious-Metal-Free Bifunctional Oxygen Electrocatalysts: Rational Design and Applications in Zn-Air Batteries, *Adv. Funct. Mater.* 28 (2018) 1803329.
- [11] J. Han, H. Bao, J.Q. Wang, L. Zheng, S. Sun, Z.L. Wang, C. Sun, 3D N-doped ordered mesoporous carbon supported single-atom Fe-N-C catalysts with superior performance for oxygen reduction reaction and zinc-air battery, *Appl. Catal. B* 280 (2021) 119411.
- [12] H. Tian, A.L. Song, P. Zhang, K.A. Sun, J.J. Wang, B. Sun, Q.H. Fan, G.J. Shao, C. Chen, H. Liu, Y.D. Li, G.X. Wang, High durability of Fe-N-C single-atom catalysts with carbon vacancies toward the oxygen reduction reaction in alkaline media, *Adv. Mater.* 35 (2023) 2210714.
- [13] C. Zhou, X. Chen, S. Liu, Y. Han, H. Meng, Q. Jiang, S. Zhao, F. Wei, J. Sun, T. Tan, R. Zhang, Superdurable bifunctional oxygen electrocatalyst for high-performance zinc-air batteries, *J. Am. Chem. Soc.* 144 (2022) 2694–2704.
- [14] T. Sun, S. Mitchell, J. Li, P. Lyu, X. Wu, J. Perez-Ramirez, J. Lu, Design of local atomic environments in single-atom electrocatalysts for renewable energy conversions, *Adv. Mater.* 33 (2021) 2003075.
- [15] K. Gong, F. Du, Z. Xia, M. Durstock, L. Dai, Nitrogen-doped carbon nanotube arrays with high electrocatalytic activity for oxygen reduction, *Science* 323 (2009) 760–764.
- [16] L. Dai, Y. Xue, L. Qu, H.J. Choi, J.B. Baek, Metal-free catalysts for oxygen reduction reaction, *Chem. Rev.* 115 (2015) 4823–4892.
- [17] Y. Zhu, Q. Lin, Y. Zhong, H.A. Tahini, Z. Shao, H. Wang, Metal oxide-based materials as an emerging family of hydrogen evolution electrocatalysts, *Energy Environ. Sci.* 13 (2020) 3361–3392.
- [18] M. Goerlin, P. Chernev, J.F. de Araujo, T. Reier, S. Dresp, B. Paul, R. Krahnert, H. Dau, P. Strasser, Oxygen evolution reaction dynamics, faradaic charge efficiency, and the active metal redox states of Ni-Fe oxide water splitting electrocatalysts, *J. Am. Chem. Soc.* 138 (2016) 5603–5614.
- [19] P. Chen, T. Zhou, L. Xing, K. Xu, Y. Tong, H. Xie, L. Zhang, W. Yan, W. Chu, C. Wu, Y. Xie, Atomically dispersed iron-nitrogen species as electrocatalysts for bifunctional oxygen evolution and reduction reactions, *Angew. Chem. Int. Ed.* 56 (2017) 610–614.
- [20] L. Yan, P. Li, Q. Zhu, A. Kumar, K. Sun, S. Tian, X. Sun, Atomically precise electrocatalysts for oxygen reduction reaction, *Chem* 9 (2023) 280–342.
- [21] P. Zhang, K. Chen, J. Li, M. Wang, M. Li, Y. Liu, Y. Pan, Bifunctional single atom catalysts for rechargeable zinc-air batteries: from dynamic mechanism to rational design, *Adv. Mater.* 35 (2023) 2303243.
- [22] L.P. Yang, X. Zhang, L.X. Yu, J.H. Hou, Z. Zhou, R.T. Lv, Atomic Fe-N₄/C in flexible carbon fiber membrane as binder-free air cathode for Zn-air batteries with stable cycling over 1000h, *Adv. Mater.* 34 (2022) 2105410.
- [23] L. Yang, L. Yu, Z.H. Huang, F. Kang, R. Lv, ZnS-assisted evolution of N, S-doped hierarchical porous carbon nanofiber membrane with highly exposed Fe-N₄/C sites for rechargeable Zn-air battery, *J. Energy Chem.* 75 (2022) 430–440.
- [24] X. Lin, Y.C. Huang, Z. Hu, L. Li, J. Zhou, Q. Zhao, H. Huang, J. Sun, C.W. Pao, Y. C. Chang, H.J. Lin, C.T. Chen, C.L. Dong, J.Q. Wang, L. Zhang, 5f covalency synergistically boosting oxygen evolution of UCoO₄ catalyst, *J. Am. Chem. Soc.* 144 (2022) 416–423.
- [25] X. Ren, T. Wu, Y. Sun, Y. Li, G. Xian, X. Liu, C. Shen, J. Gracia, H.J. Gao, H. Yang, Z. J. Xu, Spin-polarized oxygen evolution reaction under magnetic field, *Nat. Commun.* 12 (2021) 2608.
- [26] Q. Wang, S. Kaushik, X. Xiao, Q. Xu, Sustainable zinc-air battery chemistry: advances, challenges and prospects, *Chem. Soc. Rev.* 52 (2023) 6139–6190.
- [27] B. Hwang, E.S. Oh, K. Kim, Observation of electrochemical reactions at Zn electrodes in Zn-air secondary batteries, *Electrochim. Acta* 216 (2016) 484–489.
- [28] Z. Chen, A. Yu, D. Higgins, H. Li, H. Wang, Z. Chen, Highly active and durable core-corona structured bifunctional catalyst for rechargeable metal-air battery application, *Nano Lett.* 12 (2012) 1946–1952.
- [29] V. Neburchilov, H. Wang, J.J. Martin, W. Qu, A review on air cathodes for zinc-air fuel cells, *J. Power Sources* 195 (2010) 1271–1291.
- [30] Y.P. Li, W.T. Wang, M.Y. Cheng, Y.F. Feng, X. Han, Q.Z. Qian, Y. Zhu, G.Q. Zhang, Arming Ru with oxygen-vacancy-enriched RuO₂ Sub-nanometer skin activates superior bifunctionality for pH-universal overall water splitting, *Adv. Mater.* 35 (2023) 2206351.
- [31] D. Li, Z.Y. Li, Z.X. Chen, G. Shi, L. Wang, Z.H. Chen, W.G. Tu, R.D. Xia, E.I. Iwuoja, C.F. Liu, X.W. Peng, Wood-derived, monolithic chainmail electrocatalyst for biomass-assisted hydrogen production, *Adv. Energy Mater.* 13 (2023) 2300427.
- [32] H. Zhang, C. Wang, H. Luo, J. Chen, M. Kuang, J. Yang, Iron nanoparticles protected by chainmail-structured graphene for durable electrocatalytic nitrate reduction to nitrogen, *Angew. Chem. Int. Ed.* 62 (2022) e202217071.
- [33] D. Deng, L. Yu, X. Chen, G. Wang, L. Jin, X. Pan, J. Deng, G. Sun, X. Bao, Iron encapsulated within pod-like carbon nanotubes for oxygen reduction reaction, *Angew. Chem. Int. Ed.* 52 (2013) 371–375.
- [34] M. Miao, R. Hou, Z. Liang, R. Qi, T. He, Y. Yan, K. Qi, H. Liu, G. Feng, B.Y. Xia, Chainmail catalyst of ultrathin P-doped carbon shell-encapsulated nickel phosphides on graphene towards robust and efficient hydrogen generation, *J. Mater. Chem. A* 6 (2018) 24107–24113.
- [35] J. Deng, L. Yu, D. Deng, X. Chen, F. Yang, X. Bao, Highly active reduction of oxygen on a FeCo alloy catalyst encapsulated in pod-like carbon nanotubes with fewer walls, *J. Mater. Chem. A* 1 (2013) 14868–14873.
- [36] X. Cui, P. Ren, D. Deng, J. Deng, X. Bao, Single layer graphene encapsulating non-precious metals as high-performance electrocatalysts for water oxidation, *Energy Environ. Sci.* 9 (2016) 123–129.
- [37] T. Zhang, J. Bian, Y. Zhu, C. Sun, FeCo Nanoparticles Encapsulated in N-Doped Carbon Nanotubes Coupled with Layered Double (Co, Fe) Hydroxide as an Efficient Bifunctional Catalyst for Rechargeable Zinc-Air Batteries, *Small* 17 (2021) 2103737.
- [38] Z. Yang, M. Li, S. Chen, S. Yang, F. Peng, J. Liao, Y. Fang, S. Zhang, S. Zhang, Cocatalyst Engineering with Robust Tunable Carbon-Encapsulated Mo-Rich Mo/Mo₂C Heterostructure Nanoparticle for Efficient Photocatalytic Hydrogen Evolution, *Adv. Funct. Mater.* 33 (2023) 2212746.
- [39] T. Yang, Y. Huang, L. Yang, X. Li, X. Wang, G. Zhang, Y. Luo, J. Jiang, Protecting single atom catalysts with graphene/carbon-nitride "Chainmail", *J. Phys. Chem. Lett.* 10 (2019) 3129–3133.
- [40] Y. Wang, P. Ren, J. Hu, Y. Tu, Z. Gong, Y. Cui, Y. Zheng, M. Chen, W. Zhang, C. Ma, L. Yu, F. Yang, Y. Wang, X. Bao, D. Deng, Electron penetration triggering interface activity of Pt-graphene for CO oxidation at room temperature, *Nat. Commun.* 12 (2021) 5814.
- [41] T. Beyazay, K.S. Belthle, C. Fares, M. Preiner, J. Moran, W.F. Martin, H. Tuysuz, Ambient temperature CO₂ fixation to pyruvate and subsequently to citramalate over iron and nickel nanoparticles, *Nat. Commun.* 14 (2023) 570.
- [42] K. Hata, D.N. Futaba, K. Mizuno, T. Namai, M. Yumura, S. Iijima, Water-Assisted Highly Efficient Synthesis of Impurity-Free Single-Walled Carbon Nanotubes, *Science* 306 (2004) 1362–1364.
- [43] B. Mutz, M. Belimov, W. Wang, P. Sprenger, M.A. Serrer, D. Wang, P. Pfeifer, W. Kleist, J.D. Grunwaldt, Potential of an alumina-supported Ni₃Fe catalyst in the methanation of CO₂: impact of alloy formation on activity and stability, *ACS Catal.* 7 (2017) 6802–6814.
- [44] Y. Li, Z.S. Wu, P. Liu, X. Wang, W. Liu, Z. Liu, J. Ma, W. Ren, Z. Jiang, X. Bao, High-valence nickel single-atom catalysts coordinated to oxygen sites for extraordinarily activating oxygen evolution reaction, *Adv. Sci.* 7 (2020) 1903089.
- [45] J.B. Zhu, M.L. Xiao, D.Z. Ren, R. Gao, X.Z. Liu, Z. Zhang, D. Luo, W. Xing, D. Su, A. P. Yu, Z.W. Chen, Quasi-covalently coupled Ni-Cu atomic pair for synergistic electroreduction of CO₂, *J. Am. Chem. Soc.* 144 (2022) 9661–9671.
- [46] X. Ao, W. Zhang, Z. Li, J.G. Li, L. Soule, X. Huang, W.H. Chiang, H.M. Chen, C. Wang, M. Liu, X.C. Zeng, Markedly enhanced oxygen reduction activity of single-atom Fe catalysts via integration with Fe nanoclusters, *ACS Nano* 13 (2019) 11853–11862.
- [47] T. Marshall-Roth, N.J. Libretto, A.T. Wrobel, K.J. Anderton, M.L. Pegis, N.D. Ricke, T. Van Voorhis, J.T. Miller, Y. Surendranath, A pyridinic Fe-N₄ macrocycle models the active sites in Fe/N-doped carbon electrocatalysts, *Nat. Commun.* 11 (2020) 5283.
- [48] L. Zhao, Y. Zhang, L.B. Huang, X.Z. Liu, Q.H. Zhang, C. He, Z.Y. Wu, L.J. Zhang, J. Wu, W. Yang, L. Gu, J.S. Hu, L.J. Wan, Cascade anchoring strategy for general mass production of high-loading single-atomic metal-nitrogen catalysts, *Nat. Commun.* 10 (2019) 1278.
- [49] A. Han, W.M. Sun, X. Wan, D.D. Cai, X.J. Wang, F. Li, J.L. Shui, D.S. Wang, Construction of Co₄ atomic clusters to enable Fe-N₄ motifs with highly active and durable oxygen reduction performance, *Angew. Chem. Int. Ed.* 62 (2023) e202303185.
- [50] H. Meng, B. Wu, D. Zhang, X. Zhu, S. Luo, Y. You, K. Chen, J. Long, J. Zhu, L. Liu, S. Xi, T. Petit, D. Wang, X.M. Zhang, Z.J. Xu, L. Mai, Optimizing electronic synergy of atomically dispersed dual-metal Ni-N₄ and Fe-N₄ sites with adjacent Fe nanoclusters for high-efficiency oxygen electrocatalysis, *Energy Environ. Sci.* 17 (2024) 704–716.
- [51] M. Liu, Q. Chen, X. Cao, D. Tan, J. Ma, J. Zhang, Physicochemical confinement effect enables high-performing zinc-iodine batteries, *J. Am. Chem. Soc.* 144 (2022) 21683–21691.
- [52] W. Luo, Y. Wang, L. Luo, S. Gong, M. Wei, Y. Li, X. Gan, Y. Zhao, Z. Zhu, Z. Li, Single-Atom and Bimetallic Nanoalloy Supported on Nanotubes as a Bifunctional Electrocatalyst for Ultrahigh-Current-Density Overall Water Splitting, *ACS Catal.* 12 (2022) 1167–1179.
- [53] Y. Liu, C. Li, C. Tan, Z. Pei, T. Yang, S. Zhang, Q. Huang, Y. Wang, Z. Zhou, X. Liao, J. Dong, H. Tan, W. Yan, H. Yin, Z.Q. Liu, J. Huang, S. Zhao, Electrosynthesis of

- chlorine from seawater-like solution through single-atom catalysts, *Nat. Commun.* 14 (2023) 2475.
- [54] G. Wu, K.L. More, C.M. Johnston, P. Zelenay, High-Performance Electrocatalysts for Oxygen Reduction Derived from Polyaniline, Iron, and Cobalt, *Science* 332 (2011) 443–447.
- [55] Y. Tian, Z. Wu, M. Li, Q. Sun, H. Chen, D. Yuan, D. Deng, B. Johannessen, Y. Wang, Y. Zhong, L. Xu, J. Lu, S. Zhang, Atomic modulation and structure design of Fe-N₄ modified hollow carbon fibers with encapsulated Ni nanoparticles for rechargeable Zn-Air batteries, *Adv. Funct. Mater.* 32 (2022) 2209273.
- [56] J.Z. Guo, P.F. Wang, X.L. Wu, X.H. Zhang, Q.Y. Yan, H. Chen, J.P. Zhang, Y.G. Guo, High-energy/power and low-temperature cathode for sodium-ion batteries: In Situ XRD study and superior full-cell performance, *Adv. Mater.* 29 (2017) 1701968.
- [57] M. Li, B. Li, F. Meng, J. Liu, Z. Yuan, C. Wang, J. Liu, Highly sensitive and selective butanol sensors using the intermediate state nanocomposites converted from β-FeOOH to α-Fe₂O₃, *Sens. Actuators B Chem.* 273 (2018) 543–551.
- [58] H. Song, X. Zhang, T. Chen, X. Jia, One-pot synthesis of bundle-like β-FeOOH nanorods and their transformation to porous α-Fe₂O₃ microspheres, *Ceram. Int.* 40 (2014) 15595–15602.
- [59] C. Wei, Z. Nan, Effects of experimental conditions on one-dimensional single-crystal nanostructure of β-FeOOH, *Mater. Chem. Phys.* 127 (2011) 220–226.
- [60] J. Xu, X. Li, Z. Ju, Y. Sun, X. Jiao, J. Wu, C. Wang, W. Yan, H. Ju, J. Zhu, Y. Xie, Visible-light-driven overall water splitting boosted by tetrahedrally coordinated blende Cobalt(II) oxide atomic layers, *Angew. Chem. Int. Ed.* 58 (2019) 3032–3036.
- [61] W. Cheng, H. Su, Q. Liu, Tracking the oxygen dynamics of solid-liquid electrochemical interfaces by correlative *in situ* synchrotron spectroscopies, *Acc. Chem. Res.* 55 (2022) 1949–1959.
- [62] Q. Ji, Y. Kong, C. Wang, H. Tan, H. Duan, W. Hu, G. Li, Y. Lu, N. Li, Y. Wang, J. Tian, Z. Qi, Z. Sun, F. Hu, W. Yan, Lattice strain induced by linker scission in metal-organic framework nanosheets for oxygen evolution reaction, *ACS Catal.* 10 (2020) 5691–5697.